ACS Catalysis

pubs.acs.org/acscatalysis

Research Article

Hollow-ZrO_2@CuZnAl-LDH-Derived Catalyst for Direct CO_2 Hydrogenation to Methanol

Emma L. Southall, Gerardo T. Martinez, Roland C. Turnell-Ritson, and Dermot O'Hare*

Cite This: *ACS Catal.* 2026, 16, 9509−9519

Read Online

ACCESS | Metrics & More | Article Recommendations | Supporting Information

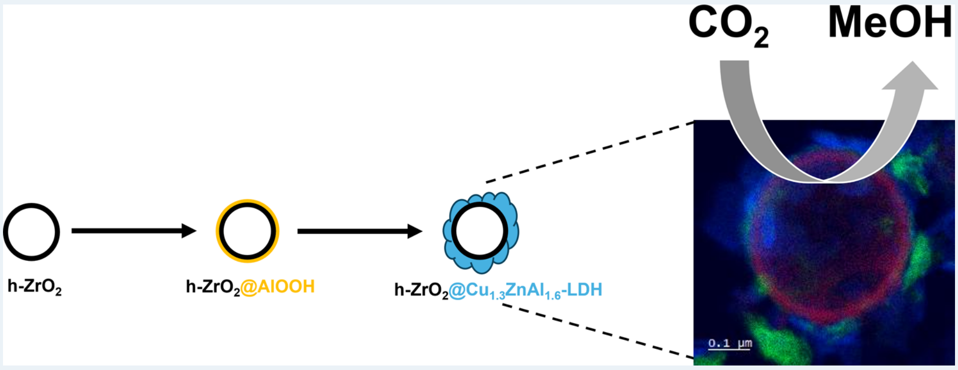

ABSTRACT: Realizing net-zero emissions demands the design of innovative and efficient catalysts for CO_2 valorization. Herein, we report a core@shell-structured catalyst precursor, h-ZrO_2@$Cu_{1.3}ZnAl_{1.6}$-LDH, in which layered double hydroxide (LDH) platelets are arranged around hollow zirconia spheres (h-ZrO_2), maximizing the interfacial area between the active LDH component and zirconia promoter. The h-ZrO_2@$Cu_{1.3}ZnAl_{1.6}$-LDH-derived catalyst efficiently converts CO_2 into methanol, reaching space-time yields (STYs) comparable to commercial catalysts, despite a 54% reduction in Cu loading (0.59 $g_{MeOH}\ g_{cat}^{-1}\ h^{-1}$ at 250 °C, 45 bar, $H_2/CO_2 = 3$, 18,000 mL $g^{-1}\ h^{-1}$ weight hourly space velocity, WHSV). Reporting the STY on a per gram copper basis highlights the efficiency of the catalyst: h-ZrO_2@$Cu_{1.3}ZnAl_{1.6}$-LDH is twofold more active than the commercial catalyst under the same conditions (2.7 *vs* 1.3 $g_{MeOH}\ g_{cat}^{-1}\ h^{-1}$).

KEYWORDS: *core@shell, CCU, CO_2 hydrogenation, layered double hydroxide, zirconia, methanol synthesis*

INTRODUCTION

Urgent developments are required to effectively combat CO_2 emissions and mitigate the most serious consequences of global warming. Carbon capture and utilization (CCU) provides a blueprint for a circular carbon economy, converting captured CO_2 into value-added carbon-containing products.[1] Among various CO_2 utilization approaches, the direct transformation of CO_2 to methanol (CTM) is widely recognized as one of the most promising candidates for large-scale deployment.[1] Indeed, demonstrations of CTM at both pilot- and commercial-scale have already been reported.[2−5] Yet, of the more than 100 million metric tons produced each year, less than 0.2% of global methanol production is renewable.[6,7] Instead, industrial production of this highly versatile chemical occurs largely *via* hydrogenation of CO_2-containing syngas.[8] This reliance on non-renewable feedstocks has contributed to a rise in CO_2 emissions associated with growing methanol production over the past decade.[9,10]

Methanol synthesis catalysts containing Cu, ZnO and Al_2O_3 have been used commercially since the 1960s.[8,11] Copper is widely acknowledged to be the primary active site, with ZnO and AlO_x species acting as promoters through mechanisms that have been debated for decades.[8] Recent work on well-defined model CuZn systems has shown that Zn-stabilized cationic Cu species can be relevant to CO_2 hydrogenation to methanol, and that formate-containing pathways can dominate in such systems.[12,13] Among a vast array of structures and synthesis methods, catalysts with easily accessible and well-dispersed copper sites demonstrate the highest activity, while maximizing the Cu/ZnO interface is responsible for high methanol selectivity.[14,15] Recently, however, the International Energy Agency (IEA) has identified 'major risks facing copper markets', forecasting a

Received: March 11, 2026
Revised: April 24, 2026
Accepted: April 27, 2026
Published: May 6, 2026

https://doi.org/10.1021/acscatal.6c01304

30% shortfall in supply by 2035.[16] Developing materials that demonstrate activities similar to well-established industrial catalysts (typically 40−50 wt % Cu), but require lower copper loadings, is therefore an important goal.

Layered double hydroxide (LDH) derived materials have shown potential as precursors to CTM catalysts.[17,18] This class of anionic clay can be described by the generic formula $[M^{II}_{1-x}M^{III}_{x}(OH)_2]^{x+}[(A^{n-})_{x/n}]\cdot mH_2O$, these materials contain positively charged layers of mixed metal ($M^{II}_{1-x}M^{III}_{x}$) octahedra held together by anions and water molecules in the interlayer galleries.[19] Advantageously, LDH-derived methanol synthesis catalysts containing only around 20 wt % of the active Cu component have demonstrated good catalytic activity.[20] Upon activation, well-dispersed Cu^0 nanoparticles are formed, which enhance catalytic performance due to the high available copper surface area.[17] Excellent atomic-scale dispersion of Cu^0 nanoparticles dispersed within ZnO afforded by the LDH-derived structure also improves methanol selectivity.[21,22] However, LDH materials are known to suffer from agglomeration due to the strong electrostatic interactions and hydrogen-bonding network present in the material, reducing accessible surface area and hindering catalytic performance. The post-synthetic aqueous-miscible organic solvent treatment (AMOST) was developed to minimize this issue. AMOST involves disrupting the hydrogen-bonding network between the layers by replacing the interlayer water molecules with less hydrophilic solvent molecules (e.g., acetone, ethanol).[23] Unfortunately, this process requires large volumes of organic solvent, making scale-up challenging. An alternative approach to reducing LDH aggregation involves anchoring LDH platelets onto an oxide support, generating hierarchical core@LDH-shell structured catalysts.[24] Previous work in our group has demonstrated the potential of such materials for the CTM reaction with LDH-coated silica particles, $SiO_2@Cu_{1.3}ZnAl$-LDH, demonstrating a methanol space-time yield (STY) of almost 0.7 $g_{MeOH}\ g_{cat}^{-1}\ h^{-1}$.[20] Subsequent work then removed the inactive silica core, in an attempt to improve the activity per unit mass of the catalyst. For reasons of synthetic practicality, Mg was included within the LDH shell, generating a hollow-$SiO_2@Cu_xZn_yMg_zAl$-LDH material.[25] This hollow-$SiO_2@Cu_xZn_yMg_zAl$-LDH material is reported to outperform a commercial catalyst, although only under certain conditions and metrics: at temperatures exceeding 270 °C (30 bar, 1:3 CO_2:H_2) and when STY is considered on a per gram copper, rather than a per gram catalyst, basis.[25]

Herein, we report a core@shell structured material, h-$ZrO_2@Cu_{1.3}ZnAl_{1.6}$-LDH, in which the LDH shell is supported on a hollow zirconia sphere, h-ZrO_2. Introducing zirconium to a CuZnAl-based catalyst is widely recognized to improve performance and stability, which is generally attributed to increased metal dispersion and the promotion of CO_2 activation *via* altered surface basicity.[26,27] Moreover, the replacement of Al_2O_3 in $CuO/ZnO/Al_2O_3$ with ZrO_2 has garnered increasing interest, as ZrO_2 is less hydrophilic than Al_2O_3 and can thus hinder deactivation of the catalyst by water.[28,29]

EXPERIMENTAL SECTION

Synthesis of h-ZrO_2 and $SiO_2@ZrO_2$

Ethanol (230 mL), ammonia (35%, 58 mL) and water (32 mL) were heated to 30 °C. Tetraethyl orthosilicate (12.6 mL, 0.056 mol) was added under vigorous stirring and left to age for 1 h. The resulting silica spheres were collected by centrifugation, washed four times with water, and then four times with ethanol, before being re-dispersed in ethanol (380 mL) for 1.5 h. The re-dispersed silica spheres were then heated to 30 °C, before an aqueous solution of Lutensol A05 (BASF, 3.76 wt %, 1.5 mL) was added under vigorous stirring. After 1 h, zirconium(IV) butoxide in butanol (80 wt %, 5.4 mL, 0.014 mol) was added. The resulting suspension was left to stir vigorously overnight, before being collected by centrifugation and washed twice with ethanol. The product was re-dispersed in ethanol (80 mL), before water (276 mL) was added under vigorous stirring. After 1 h, the $SiO_2@ZrO_2$ product was collected by centrifuge, washed twice with water and dried at 60 °C overnight. The dried $SiO_2@ZrO_2$ was calcined at 900 °C for 2 h (2.5 °C/min).

h-ZrO_2 was synthesized from calcined $SiO_2@ZrO_2$ by adding NaOH (0.25 M) to $SiO_2@ZrO_2$ (100 mL/g). The suspension was kept under static conditions at 30 °C for 24 h, then collected *via* vacuum filtration and washed with water until pH = 7. The h-ZrO_2 product was dried at 60 °C overnight.

Synthesis of h-$ZrO_2@AlOOH$

h-ZrO_2 (0.28 g) was dispersed in an aluminum isopropoxide/ethanol solution (176 mL, 0.016 mol/L) for 30 min. The resulting suspension was kept at 45 °C with vigorous stirring for 16 h. An ethanol/water mixture (5/1 v/v, 140 mL) was then added and left to stir for 2 h, before the suspension was transferred to an autoclave and heated to 80 °C for 22 h. The h-$ZrO_2@AlOOH$ product was collected *via* filtration, washed with ethanol/water (5/1 v/v) and dried at 60 °C overnight.

Synthesis of h-$ZrO_2@Cu_{1.3}ZnAl_{1.6}$-LDH, $CuO/Cu_xZn_yAl_z$-LDH, and $Cu_{1.3}ZnAl$-LDH

h-$ZrO_2@Cu_{1.3}ZnAl_{1.6}$-LDH, $CuO/Cu_xZn_yAl_z$-LDH and $Cu_{1.3}ZnAl$-LDH were prepared by co-precipitation.

h-$ZrO_2@Cu_{1.3}ZnAl_{1.6}$-LDH was prepared by adding h-$ZrO_2@AlOOH$ (0.12 g) to water (24 mL). After 30 min of sonication, sodium carbonate (0.0034 g) was added with 5 min of continued sonication. If required, the pH was adjusted to pH 10 with NaOH (1 M) after this time. Separately, copper nitrate trihydrate (0.19 g, 0.80 mmol), zinc nitrate hexahydrate (0.20 g, 0.67 mmol) and aluminum nitrate nonahydrate (0.088 g, 0.23 mmol) were dissolved in water (24 mL). The aqueous metal nitrate solution was then added to the h-ZrO_2/Na_2CO_3 mixture (1 mL/min, 500 rpm) and the pH was maintained at pH 10 by the simultaneous dropwise addition of NaOH (1 M). The resulting suspension was aged at room temperature for 1.5 h, then collected by filtration and washed with water until pH 7. The h-$ZrO_2@Cu_{1.3}ZnAl_{1.6}$-LDH product was dried at 50 °C overnight.

CuO/Cu_xZnAl-LDH was prepared using the same procedure as detailed for the synthesis of h-$ZrO_2@Cu_{1.3}ZnAl_{1.6}$-LDH, but in the absence of h-$ZrO_2@AlOOH$ (i.e., the metal nitrate solution was added to an aqueous solution of Na_2CO_3).

$Cu_{1.3}ZnAl$-LDH was prepared using the same procedure as for the synthesis of $CuO/Cu_xZn_yAl_z$-LDH, but using altered masses of copper nitrate trihydrate (0.17 g, 0.70 mmol), zinc nitrate hexahydrate (0.16 g, 0.54 mmol) and aluminum nitrate nonahydrate (0.20 g, 0.53 mmol).

Calcination

The LDH/LDH-based core@shell was converted into the corresponding layered double oxide (LDO) *via* calcination in air. A step method was used (10 °C/min to 80 °C, dwell 1 h; 10 °C/min to 150 °C, dwell for 1 h; 10 °C/min to 330 °C, dwell for 3 h), with an air flow of 50 mL/min at ambient pressure.

CATALYST CHARACTERIZATION

Transmission Electron Microscopy (TEM)

TEM images and STEM-EDX mapping in Figure 1A (and Figures S1, S6, S7, S9, S10, S13, and S18) were collected on a

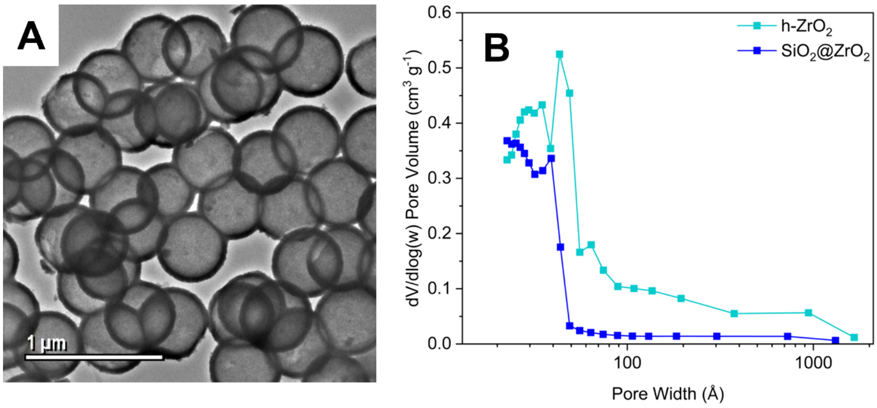

Figure 1. (A) TEM image of h-ZrO_2 formed following the synthesis described in Scheme 1 (i.e., using 0.25 M NaOH at 30 °C during the hollowing procedure). (B) BJH desorption plots of h-ZrO_2 and SiO_2@ZrO_2, highlighting the creation of mesopores during the hollowing process.

JEOL 2100 instrument using a tungsten filament. An accelerating voltage of 200 kV and single tilt specimen holder were used. Samples were prepared by drop casting an aqueous suspension of the sample onto carbon-coated nickel grids.

Scanning Transmission Electron Microscopy and Energy Dispersive Spectroscopy (STEM-EDS)

Scanning Transmission Electron Microscopy and Energy Dispersive Spectroscopy (STEM-EDS) characterization was performed using a JEM-ARM300F2 GRAND ARM microscope equipped with double SSD EDS detectors working at 300 kV acceleration voltage. The sample was drop casted onto a TEM gold grid with carbon support, which was mounted in a High-Count-Analytical Double Tilt holder to optimize for EDS counts and reduce instrument spurious signals.

Powder X-ray Diffraction (PXRD)

PXRD experiments were performed on a Brucker D8 ECO diffractometer, with Cu Kα radiation (λ = 1.5418 Å, 45 kV, 40 mA). The sample was packed on a PMMA holder, and patterns were collected between $2\theta = 5 - 70°$ in continuous measuring mode for a total time of 25 min, with data points taken every 0.0115°. Synchrotron data were collected on the I11 beamline at Diamond Light Source, UK.

Inductively Coupled Plasma-Optical Emission Spectroscopy (ICP-OES)

To facilitate comparisons between samples, ICP-OES measurements were performed on the calcined samples (i.e., the corresponding LDOs). The ICP-OES data for h-ZrO_2@$Cu_{1.3}ZnAl_{1.6}$-LDO was calculated from an average of 3 samples.

Thermal Gravimetric Analysis (TGA)

TGA was carried out on a PerkinElmer TGA 800 instrument. Approximately 10 mg of sample was heated between 30 and 800 °C at 5 °C/min under a nitrogen atmosphere.

N_2 Brauner-Emmett-Teller (BET)

Nitrogen adsorption/desorption isotherms were collected at −196 °C on a Micromeritics Tristar II instrument. The Barrett-Joyner-Halenda (BJH) method was used to calculate pore widths from the desorption data obtained. Prior to measurement, each sample was calcined in air (50 mL/min) using a step method (10 °C/min to 80 °C, dwell 1 h; 10 °C/min to 150 °C, dwell for 1 h; 10 °C/min to 330 °C, dwell for 3 h). The calcined sample was then degassed under vacuum at 110 °C overnight.

H_2 Temperature-Programmed Reduction (H_2-TPR)

H_2-TPR profiles were measured using a Micromeritics Autochem II 2920 Chemisorption Analyser equipped with a thermal conductivity detector (TCD). Prior to measurement, each sample was calcined in air (50 mL/min) using a step method (10 °C/min to 80 °C, dwell 1 h; 10 °C/min to 150 °C, dwell for 1 h; 10 °C/min to 330 °C, dwell for 3 h), then loaded into a quartz U-tube. The sample was pre-treated with He for 5 min at room temperature, before heating to 150 °C (10 °C/min, 5 min dwell) to remove moisture. Once cooled to 40 °C, the sample was heated to 400 °C under 10% H_2/N_2 and a measurement was taken every 1 s.

N_2O Chemisorption Experiments for Cu Surface Area

N_2O chemisorption experiments were performed on a Micromeritics Autochem II 2920 Chemisorption Analyser equipped with a thermal conductivity detector (TCD). Prior to measurement, each sample was calcined in air (50 mL/min) using a step method (10 °C/min to 80 °C, dwell 1 h; 10 °C/min to 150 °C, dwell for 1 h; 10 °C/min to 330 °C, dwell for 3 h), then loaded into a quartz U-tube. Copper surface area and dispersion were determined using a two-step H_2-TPR method. Initially, the sample was pre-treated with He for 5 min at room temperature, before heating to 150 °C (10 °C/min, 5 min dwell) to remove moisture. Once cooled to 40 °C, the sample was heated to 300 °C under 10% H_2/N_2 and a measurement was taken every 1 s. The hydrogen consumption was recorded (area = A_1). The sample was then cooled to 65 °C and exposed to N_2O for 1 h. A second H_2-TPR experiment was then performed using an identical program and the hydrogen consumption was measured (area = A_2).

Copper dispersion (D_{Cu}) was calculated from:

$$D_{Cu} = \frac{2A_2}{A_1}$$

Copper surface area (S_{Cu}) was calculated by:

$$S_{Cu} = \frac{D_{Cu} \times N_{Av} \times \mathrm{Cu(wt\,\%)}}{100 \times \mathrm{MW}_{Cu} \times N_{Cu}}$$

where N_{Av} is Avogadro's number, MW_{Cu} is the molar mass of copper (63.5 g mol^{-1}) and N_{Cu} is a reported value for the surface atom density of copper (1.7×10^{19} m^{-2}).[30]

Temperature-Programmed Desorption with CO_2 (CO_2-TPD)

CO_2-TPD experiments were performed on a Micromeritics Autochem II 2920 Chemisorption Analyser equipped with a thermal conductivity detector (TCD). Prior to measurement, each sample was calcined in air (50 mL/min) using a step method (10 °C/min to 80 °C, dwell 1 h; 10 °C/min to 150 °C, dwell for 1 h; 10 °C/min to 330 °C, dwell for 3 h), then loaded into a quartz U-tube. The sample was pre-treated with He for 10 min at room temperature, before heating to 150 °C (10 °C/min, 10 min dwell) to remove moisture. Once cooled to 40 °C, the sample was heated to 290 °C for 2 h under 10% H_2/N_2 (5 °C/min), then cooled back to 40 °C. The sample was then exposed to CO_2 (50 mL/min) for 1 h. Excess CO_2 was then cleared by flowing He (50 mL/min) for 1 h. Finally, the material was heated to 330 °C for 1 h (10 °C/min). Measurements were taken every 1 s.

Scanning Electron Microscopy Energy Dispersive X-ray (SEM-EDX)

SEM-EDX was performed on a Carl Zeiss Merlin Instrument, fitted with an Oxford Instruments Xmax 150 mm^2 EDX detector. Scanning electron microscopy images were collected with an SE2 lens, at working distances of 10 mm and voltages of 4 kV. Elemental mapping was performed at a working distance of 8.5 nm. The sample was drop casted onto a carbon spot attached to a metal pin stub. A chromium layer (∼4 nm) was deposited on the sample prior to imaging.

Solid State Nuclear Magnetic Resonance Spectroscopy (SS-NMR)

^{29}Si Magic angle spinning SS-NMR spectra were obtained at 79.4 MHz (9.4 T) on a Bruker Avance IIIHD spectrometer. Samples were packed in 4 mm O.D. rotors and spun at 10 kHz. The spectra were collected using direct polarization with spinal64 proton decoupling. All ^{29}Si spectra were referenced to kaolinite (the shift taken to be at $\delta = 91.7$ ppm on a scale where $\delta(\mathrm{TMS}) = 0$) as a secondary reference.

Catalytic CO_2 Hydrogenation Experiments

Catalytic CO_2 hydrogenation to methanol tests were performed in a tubular fixed-bed reactor. Prior to the hydrogenation experiments, each sample was calcined in air (50 mL/min) using a step method (10 °C/min to 80 °C, dwell 1 h; 10 °C/min to 150 °C, dwell for 1 h; 10 °C/min to 330 °C, dwell for 3 h). 100 mg (±1 mg) of the calcined sample (350−255 μm) was then loaded into a quartz tube and reduced *in situ* (5% H_2 in N_2, 290 °C, 2 h, 4 °C/min). After cooling below 80 °C, the reactor was pressurized to 45 bar (CO_2:H_2 1:3) and the reaction was started. Products were analyzed using an Agilent 7890B gas chromatograph (GC), fitted with a thermal conductivity detector (TCD) and flame ionization detector (FID).

GC injections were taken every 45 min at temperatures between 230 and 310 °C inclusive. Four injections were taken at each temperature allowing averages and standard errors to be calculated.

■ RESULTS AND DISCUSSION

Synthesis of the Hollow Core Component

To make a uniform core@shell structured catalyst, it is first necessary to synthesize a homogeneous and uniform core component. Although the synthesis of hollow zirconia spheres (h-ZrO_2) exists in the literature, modifications were made to minimize the high proportion of broken h-ZrO_2 produced (Figure S1).[31,32]

The synthetic route to h-ZrO_2 is described in Scheme 1. Initially, silica spheres with a diameter of 490 ± 20 nm (Figure S2) were synthesized according to the well-established Stöber procedure (Scheme 1, step 1). These spheres were subsequently coated with an aqueous solution of surfactant (3.76 wt % Lutensol A05; Scheme 1, step 2(i)), before Zr(IV) butoxide was added (Scheme 1, step 2(ii)). It is important that water is added alongside the surfactant (i.e., that an aqueous surfactant solution is used), so that the surfactant traps an aqueous layer on the surface of the silica, hydrolyzing only the Zr(IV) butoxide in close proximity to the spheres. The excess, unreacted Zr(IV) butoxide is removed (Scheme 1, step 2(iii)) before completion of Zr(IV) butoxide hydrolysis (Scheme 1,

Scheme 1. Three-Step Synthesis of Hollow Zirconia Spheres (h-ZrO_2): Step 1: Synthesis of the Spherical SiO_2 Template; Step 2: Formation of the SiO_2@ZrO_2 Core@shell; Step 3: Removal of the Central SiO_2 Component, Leaving h-ZrO_2

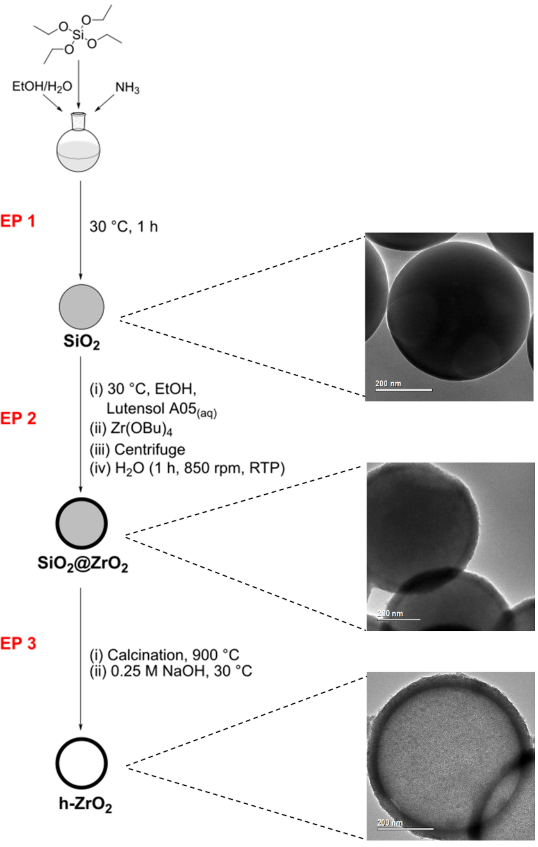

step 2(iv)). Failure to remove the excess Zr(IV) butoxide component in step 2(iii) forms a large quantity of free zirconia, which cannot be easily separated from the $SiO_2@ZrO_2$ product (Figure S3). It is noteworthy that a zirconia layer of thickness 36 ± 3 nm formed after only 1 h of hydrolysis (Figure S4), which is comparable to the thickness in previously reported $SiO_2@ZrO_2$ protocols, where the hydrolysis was performed under static conditions for three days.[32]

Calcination of $SiO_2@ZrO_2$ at 900 °C (Scheme 1, step 3(i)) yields primarily the tetragonal zirconia polymorph (Figure S5). Relative to the monoclinic phase, Cu/ZrO_2 catalysts using tetragonal-ZrO_2 are reported to exhibit higher methanol activities in the CTM reaction as a result of enhanced metal-support interactions, while other studies attribute an improvement in catalytic activity to a more dispersed active Cu component on the tetragonal-ZrO_2 support.[33,34] Furthermore, ZnO/tetragonal-ZrO_2 systems have exhibited higher methanol selectivities than analogous monoclinic systems as a result of different ZnO_x species formed.[35]

h-ZrO_2 structures are generated *via* the dissolution of the central SiO_2 component in calcined $SiO_2@ZrO_2$ (step 3(ii)). It was found that lowering the temperature to 30 °C (from 50 °C) and decreasing the NaOH concentration to 0.25 M (from 3 M) significantly reduced the number of broken spheres observed by transmission electron microscopy (TEM) imaging (Figure 1A and Figure S6).[31] Further reducing the NaOH concentration to 0.1 M, however, was insufficient to uniformly remove SiO_2 from all $SiO_2@ZrO_2$ spheres, with the central portion of several spheres still appearing very dark in bright field TEM images (Figure S6K,L). h-ZrO_2 etched using 0.25 M NaOH displayed no dark centers, but residual silicon is evidenced by scanning transmission electron microscopy energy dispersive X-ray (STEM-EDX) mapping (Figure S7) and ^{29}Si nuclear magnetic resonance (NMR) spectroscopy (Figure S8). ^{29}Si NMR spectroscopy confirmed that the Si environment was unaffected by modifications to the ZrO_2 coating procedure (Scheme 1, step 2), with only one singlet peak present at $\delta = -110$ ppm in the ^{29}Si NMR spectrum of $SiO_2@ZrO_2$ synthesized following either the literature method or the modified method described in Scheme 1 (Figure S8).[31] This peak is indicative of $(SiO)_4\mathbf{Si}$ units, i.e., Q^4 Si sites.[36] Upon hollowing, new additional Si environments at *ca.* $\delta = -97$ and -87 ppm were created, indicative of $(SiO)_3\mathbf{Si}OH$ (i.e., Q^3 sites) and $(SiO)_2\mathbf{Si}(OH)_2$ units (Q^2 sites), respectively. Interestingly, the ratio of Q^2 to Q^4 sites is smaller for h-ZrO_2 produced in this work (Scheme 1) than for previously reported methods, suggesting that modifications to the core removal step may alter the nature of residual Si-species.[31] Barrett-Joyner-Halenda (BJH) desorption plots reveal that the zirconia layer is inherently mesoporous, and becomes more so when subjected to basic conditions, with a number of small mesopores created during the hollowing procedure (pore width ~44 Å; Figure 1B). These mesopores in the zirconia shell may enhance gas flow through the catalyst and thus improve catalytic performance.

It should be noted that the h-ZrO_2 spheres do not possess high mechanical strength, and grinding with a mortar and pestle introduces fractures to previously intact spheres (Figure S9).

Development of the h-ZrO_2@LDH Structure

Core@LDH-shell structures are often synthesized using hydrothermal procedures.[37,38] However, the complexation of Cu^{2+} ions by ammonia, formed *in situ* from the decomposition of urea, precludes the application of such methods to Cu-containing LDH materials. The preparation of an LDH shell on the h-ZrO_2 cores was therefore attempted using co-precipitation, another standard LDH synthesis technique.[20,24,39] A Cu:Zn:Al (CZA) ratio of 1.3:1:1 was used based on promising previous results.[20] Unfortunately, simple co-precipitation of an aqueous CZA nitrate solution into a basic suspension of h-ZrO_2 did not result in core@shell formation. Instead, a mixture of the two components (h-ZrO_2 and LDH) was observed (Figure 2). Scanning transmission electron microscopy energy dispersive X-ray (STEM-EDX) confirmed that Cu, Zn and Al were not present in large quantities on the spheres, instead appearing primarily in the spaces between h-ZrO_2. This resembles a physical mixture (PM) of the two components, which can alternatively be prepared by combining separate samples of h-ZrO_2 and $Cu_{1.3}$ZnAl-LDH (Figure S10). The material shown in Figure 2 will be referred to as cp-h-ZrO_2+$Cu_{1.3}$ZnAl-LDH, where the ‘cp’ prefix is used to highlight that the co-precipitation method was used to prepare the sample. Such a prefix therefore distinguishes this material from h-ZrO_2+$Cu_{1.3}$ZnAl-LDH, which instead describes a sample prepared by mixing the two pre-prepared components. It should be noted, however, that while the chemical bonding between the two components in physical mixtures (PMs) is unlikely, it is probable that electrostatic interactions between the positively charged LDH platelets ($\zeta = 38.1$ mV) and negatively charged spheres ($\zeta = -35.5$ mV) hold the two components in close proximity (Figure S11).

Subsequent experimental efforts sought to encourage core@shell growth with the addition of an aluminum oxide/hydroxide layer to the outer surface of h-ZrO_2, since an Al(III) source provides nucleation sites for LDH growth.[40,41] While impregnation of h-ZrO_2 with $Al(NO_3)_3$ offers a simple route to introduce Al(III), this approach can ultimately result in irregular coverage of the shell component on the core.[42] In contrast, Shao *et al.* achieved uniform SiO_2@NiAl-LDH by forming a boehmite (aluminum oxyhydroxide, AlOOH) coating (*via* aluminum isopropoxide hydrolysis), which transforms into an LDH phase during hydrothermal synthesis.[38] A similar AlOOH coating was therefore added to h-ZrO_2, generating h-ZrO_2@AlOOH structures (Figure S13), which were then subjected to the co-precipitation step. In contrast to the morphology of cp-h-ZrO_2+$Cu_{1.3}$ZnAl-LDH, STEM-EDX confirms that a much greater proportion of the Cu, Zn and Al atoms are located on the h-ZrO_2 spheres when the co-precipitation is performed on h-ZrO_2@AlOOH, rather than on h-ZrO_2 (Figures 2 and 3),

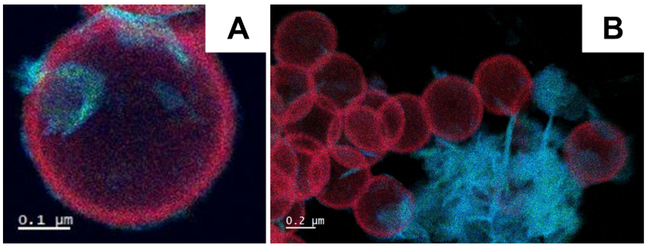

Figure 2. STEM-EDX maps of cp-h-ZrO_2+$Cu_{1.3}$ZnAl-LDH (A, B). The EDX maps are presented in RGB format, in which Zr, Al, and Cu are represented in red, green, and blue, respectively. Mapping of Zn (Figure S12) confirms that Zn appears in the same locations as Cu.

https://doi.org/10.1021/acscatal.6c01304

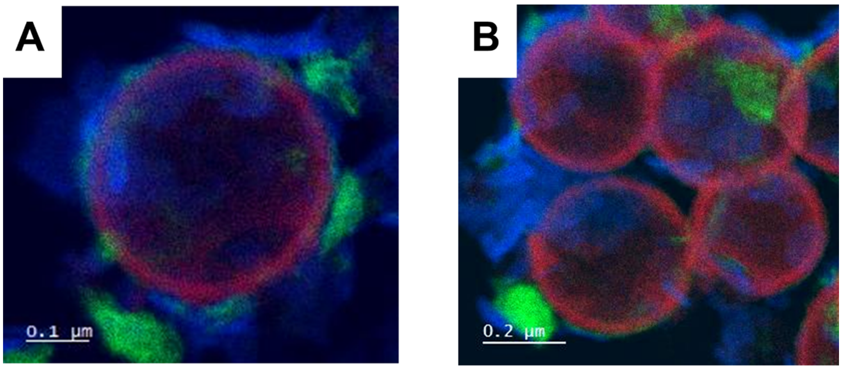

Figure 3. STEM-EDX maps of h-ZrO_2@$Cu_{1.3}ZnAl_{1.6}$-LDH (A, B), prepared by co-precipitation with h-ZrO_2@AlOOH cores. The EDX maps are presented in RGB format, in which Zr, Al, and Cu are represented in red, green, and blue, respectively. Mapping of Zn (Figure S12) confirms that Zn appears in the same locations as Cu.

suggesting h-ZrO_2@$Cu_{1.3}ZnAl_{1.6}$-LDH had been successfully synthesized.

Powder X-ray diffraction (PXRD) confirmed the presence of the LDH and tetragonal-zirconia phases (Figure 4A), with characteristic LDH Bragg reflections at 2θ = 11.6°, 23.3°, 34.5°, 39.1°, 59.9° and 61.1°, which can be indexed as the (003), (006), (012), (015), (110) and (113) reflections respectively, and characteristic tetragonal zirconia Bragg reflections at 2θ = 30.2°, 35.3°, 50.4° and 60.1°, which can be indexed as the (111), (200), (220), (311) reflections respectively. A two-phase Rietveld refinement of synchrotron powder X-ray diffraction data (Figure 4B) indicated a 42:58 wt % ratio between the ZrO_2 and LDH phases.[43] PXRD patterns confirmed the loss of the layered, crystalline LDH structure upon calcination to form the corresponding layered double oxide (LDO), and the appearance of reflections consistent with metallic Cu^0 upon subsequent reduction (Figure S14).

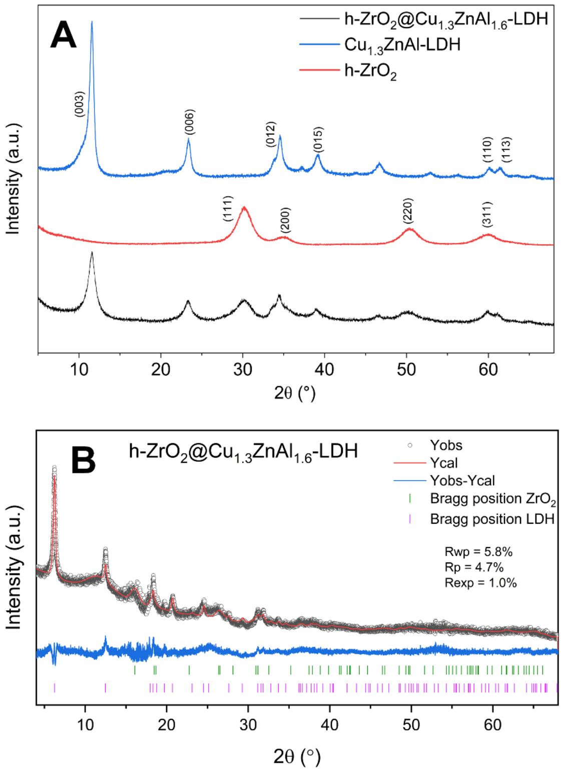

Figure 4. (A) PXRD pattern of h-ZrO_2@$Cu_{1.3}ZnAl_{1.6}$-LDH, compared to the h-ZrO_2 core and $Cu_{1.3}ZnAl$-LDH. (B) Rietveld refinement (performed using TOPAS (v6)) of h-ZrO_2@$Cu_{1.3}ZnAl_{1.6}$-LDH.

In order to account for the Al present in the AlOOH coating, a 1.2:1:0.3 ratio of Cu:Zn:Al nitrates was used during the co-precipitation with h-ZrO_2@AlOOH. The small amount of additional Al salt was needed to facilitate the LDH synthesis. This protocol yielded the product h-ZrO_2@$Cu_{1.3}ZnAl_{1.6}$-LDH, where the 1.3:1:1.6 Cu:Zn:Al molar ratio (calculated from ICP-OES data, Table S1) assumes that all Al is present in the form of the LDH (i.e., that the AlOOH coating completely transforms into the LDH phase). STEM-EDX images presented in Figure 3 highlight localized areas of Al, suggesting that some portion of the AlOOH remains alongside h-ZrO_2@$Cu_{1.3}ZnAl_{1.6}$-LDH. As a consequence, the LDH composition in h-ZrO_2@$Cu_{1.3}ZnAl_{1.6}$-LDH is not entirely homogeneous, which may affect its catalytic activity.

The BJH desorption plot of calcined h-ZrO_2@AlOOH reveals a large number of mesopores (pore width ~45 Å) relative to the amount measured for calcined h-ZrO_2 (Figure S15). It can therefore be suggested that residual AlOOH is unlikely to prevent gaseous diffusion through the catalyst during thermal testing. In the calcined $Cu_{1.3}ZnAl$-LDH, similar-sized mesopores to those present in h-ZrO_2@AlOOH coexist with larger mesopores (~295 Å, Figure 5). Interestingly, the BJH desorption plot of h-ZrO_2@$Cu_{1.3}ZnAl_{1.6}$-LDH shows a broad peak centered around 66 Å, which is absent in the plots of h-ZrO_2, h-ZrO_2@AlOOH and $Cu_{1.3}ZnAl$-LDH. The presence of a unique pore size region provides evidence of structural differences in h-ZrO_2@$Cu_{1.3}ZnAl_{1.6}$-LDH, which may be explained by the presence of an interfacial core-shell region. It can be noted that the magnitude of the peak at ~45 Å is significantly diminished in h-ZrO_2@$Cu_{1.3}ZnAl_{1.6}$-LDH compared to that in h-ZrO_2@AlOOH, suggesting a large proportion of the coating has transformed into the LDH phase.

Further evidence of residual AlOOH is provided by thermogravimetric analysis (TGA, Figure 6) and its first derivative (dTGA), which serves to magnify TGA events. Following the first two characteristic weight loss events of LDH-based materials, which represent (1) the loss of physisorbed solvent (i.e., water) below 150 °C and (2) dehydroxylation of the LDH layers and decomposition of the interlayer carbonate anions (150−350 °C), the dTGA of h-ZrO_2@$Cu_{1.3}ZnAl_{1.6}$-LDH

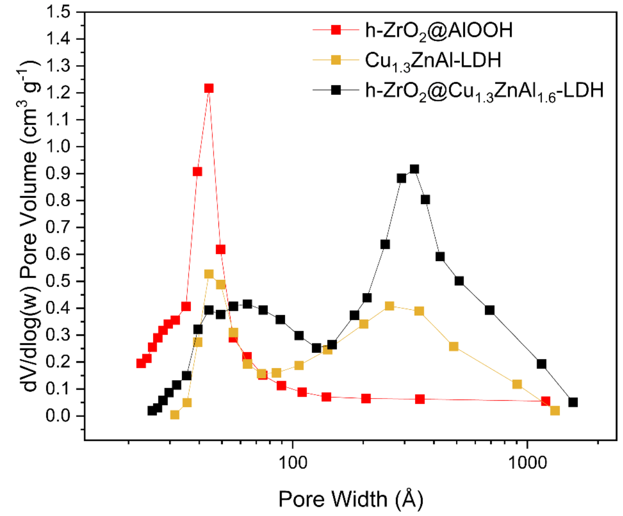

Figure 5. BJH desorption plots of h-ZrO$_2$@Cu$_{1.3}$ZnAl$_{1.6}$-LDH, Cu$_{1.3}$ZnAl-LDH, and h-ZrO$_2$@AlOOH, highlighting the difference in porosity of the core@shell sample.

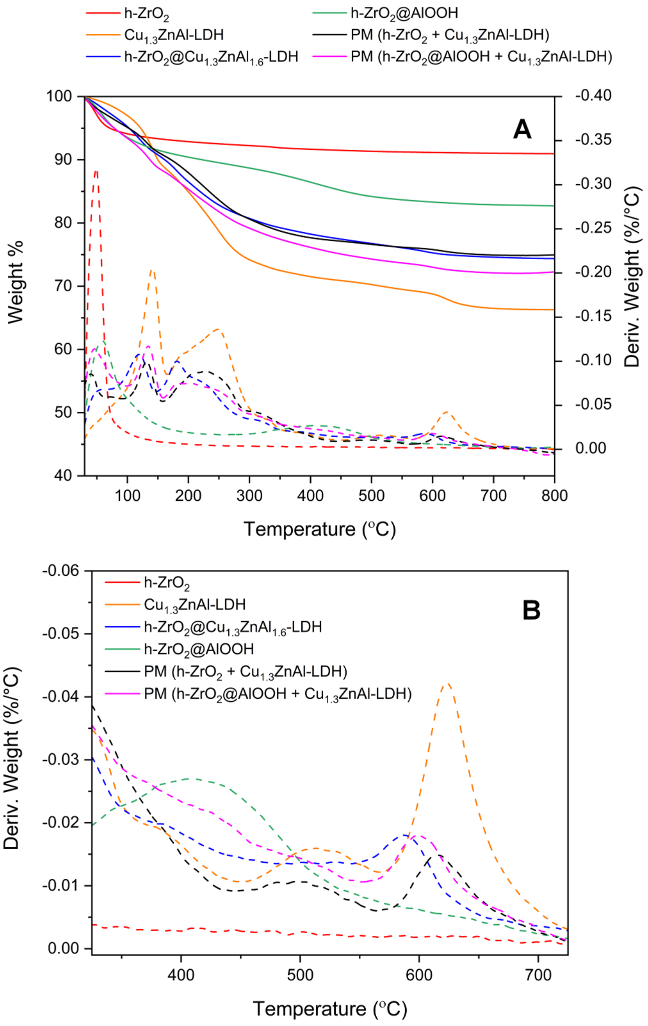

Figure 6. (A) TGA and dTGA profiles of h-ZrO$_2$@Cu$_{1.3}$ZnAl$_{1.6}$-LDH, compared to individual core and shell components and their physical mixtures (PMs), with an enlargement of the dTGA data showing the final weight loss events shown in (B).

exhibits a slight slope before returning to its baseline around 500 °C. This event is not observed in the dTGA profiles of h-ZrO$_2$ or the LDH alone, but appears in that of h-ZrO$_2$@AlOOH as a broad peak centered around 420 °C, corresponding to the decomposition of an intermediate Al(OH)$_3$ phase.[44] Notably, the magnitude of this event is significantly diminished in the core@shell sample, supporting the conclusion that the majority of the AlOOH phase is transformed into LDH during the core@-shell synthesis. The magnitude of this event is also diminished in the core@shell sample relative to a physical mixture of h-ZrO$_2$@AlOOH and LDH, again highlighting structural differences between these samples.

The final characteristic LDH decomposition event is observed at temperatures exceeding 500 °C and describes full decarbonation of carbonate anions (Figure 6B).[45] Comparison of the dTGA profiles of the physical mixture of Cu$_{1.3}$Zn$_{1.3}$Al-LDH and h-ZrO$_2$@AlOOH with the individual components reveals that the final event occurs at a lower temperature in the mixture than in the LDH alone (600 vs 616 °C). This implies that interactions between the AlOOH coating and the LDH can influence the stability of the LDH, since such a lowering in temperature of this final decomposition event is not observed in a physical mixture of h-ZrO$_2$ and Cu$_{1.3}$ZnAl-LDH. In the core@shell h-ZrO$_2$@Cu$_{1.3}$ZnAl$_{1.6}$-LDH, the final decomposition event occurs at an even lower temperature (585 °C) providing further evidence of differences in bonding between the components in the core@-shell material as compared to physical mixtures.

Performing the same co-precipitation used to synthesize h-ZrO$_2$@Cu$_{1.3}$ZnAl$_{1.6}$-LDH from h-ZrO$_2$@AlOOH (i.e., with a 1.2:1:0.3 ratio of Cu:Zn:Al nitrates), in the absence of any core component, yielded a mixed phase CuO/LDH material (Figure S16), confirming that the ratio of metal nitrates added during the synthesis is outside the range for pure phase LDH formation, without an additional source of Al. The absence of CuO reflections in the PXRD pattern of h-ZrO$_2$@Cu$_{1.3}$ZnAl$_{1.6}$-LDH therefore implies that a quantity of the AlOOH transforms to form a stable LDH phase during the synthesis.

Catalytic Performance of h-ZrO$_2$@LDH

The performance of the catalysts was evaluated for thermal CO$_2$ hydrogenation to methanol under the following conditions: 45 bar, 1:3 CO$_2$:H$_2$, 18000 mL g^{-1} h^{-1} WHSV. Prior to catalytic testing, all samples were calcined in air at 330 °C, then reduced *in situ* under H$_2$ at 290 °C. Typically, the exothermic methanol synthesis reaction is performed at moderate temperatures (200−350 °C) due to equilibrium limitations; although higher temperatures promote CO$_2$ conversion, they also favor the endothermic reverse water gas shift reaction ($\Delta H = +41.2$ kJ mol^{-1}) which converts CO$_2$ to CO, thereby reducing methanol selectivity in the exothermic CO$_2$ hydrogenation reaction ($\Delta H = -49.5$ kJ mol^{-1}).[46] Equilibrium CO$_2$ conversion (X_{CO2}) and methanol selectivity are *ca.* 30% and 90%, respectively, at 50 bar and 225 °C, using a 1:3 CO$_2$:H$_2$ feed.[46]

Under our testing conditions, h-ZrO$_2$@Cu$_{1.3}$ZnAl$_{1.6}$-LDH reaches a maximum methanol STY of 0.59 g_{MeOH} g_{cat}^{-1} h^{-1} at 250 °C (Figure S17). This represents a reduction in temperature of 20 °C compared to the peak STY reported for SiO$_2$@Cu$_{1.3}$ZnAl-LDH (0.64 g_{MeOH} g_{cat}^{-1} h^{-1}).[20] A commercial Cu/ZnO/Al$_2$O$_3$ catalyst performs similarly (0.60 g_{MeOH} g_{cat}^{-1} h^{-1}) to h-ZrO$_2$@Cu$_{1.3}$ZnAl$_{1.6}$-LDH at 250 °C, despite h-ZrO$_2$@Cu$_{1.3}$ZnAl$_{1.6}$-LDH containing ~54 wt % less copper. The superior catalytic efficiency of the core@shell is highlighted when STY is considered per gram of copper, outperforming the commercial catalyst at all temperatures studied (Figure 7). Post-testing TEM imaging revealed that the spheres remained intact, and there were no noticeable morphological changes which occurred in the shell component (Figure S18).

In comparison, hollow-SiO_2@$Cu_{1.4}ZnMg_{3.2}Al_{2.5}$-LDH, another spherical hollow structure with a comparable Cu:Zn ratio, is only reported to outperform a commercial catalyst at temperatures of 270 and 290 °C.[25] Further evidence of the enhanced copper efficiency in the core@shell structure can be found by comparison of h-ZrO_2@$Cu_{1.3}ZnAl_{1.6}$-LDH with the pure $Cu_{1.3}$ZnAl-LDH sample (Figure 8). Measurement of the Cu surface area (S_{Cu}), inferred from N_2O chemisorption measurements, indicates that activated h-ZrO_2@$Cu_{1.3}ZnAl_{1.6}$-LDH possesses a greater S_{Cu} than the activated LDH alone (48.4 and 37.9 m^2 g^{-1}, respectively, Table S2). An increased accessibility to catalytically active sites in h-ZrO_2@$Cu_{1.3}ZnAl_{1.6}$-LDH therefore rationalizes its superior performance. Furthermore, the increased S_{Cu} of the hollow-core@shell sample implies a more stable Cu dispersion as a result of the anchored platelets preventing agglomeration, which could possibly translate to improved catalyst lifetime.[20] However, time-on-stream stability studies would be necessary to confirm this effect. In addition, temperature programmed desorption experiments with CO_2 (CO_2-TPD) were performed (Table S3). The results of these indicate that h-ZrO_2@$Cu_{1.3}ZnAl_{1.6}$-LDH possesses a greater quantity of basic sites than the unsupported LDH (0.43 and 0.37 mmol g^{-1}, respectively), demonstrating enhanced CO_2 adsorption and activation ability upon incorporating the h-ZrO_2 core. Moreover, Figure S19 highlights that, despite the presence of less of the catalytically active copper component per unit mass, h-ZrO_2@$Cu_{1.3}ZnAl_{1.6}$-LDH still performs similarly to the LDH alone, when considered on a per gram catalyst basis (~22 and 35 wt % copper, respectively). h-ZrO_2 alone demonstrates very little activity under these reaction conditions, with CO_2 conversions, X_{CO2}, <5% across the temperature range studied (Figure S20A). Coating h-ZrO_2 in AlOOH slightly improves X_{CO2}, (~9%), but reduces methanol selectivity by ~40% at 250 °C (Figure S20B). The simple presence of the core component is therefore unlikely to be responsible for the improvement in catalytic activity.

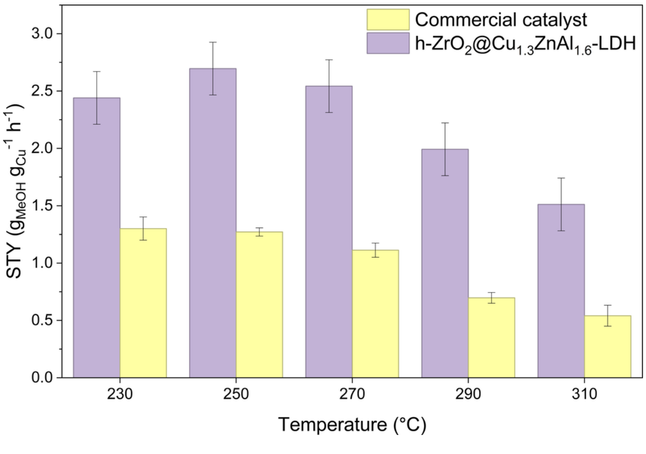

Figure 7. Catalytic testing data of h-ZrO_2@$Cu_{1.3}ZnAl_{1.6}$-LDH and a commercial methanol synthesis catalyst considered on a per gram copper basis (45 bar, 3:1 H_2:CO_2, WHSV = 18,000 mL g^{-1} h^{-1}).

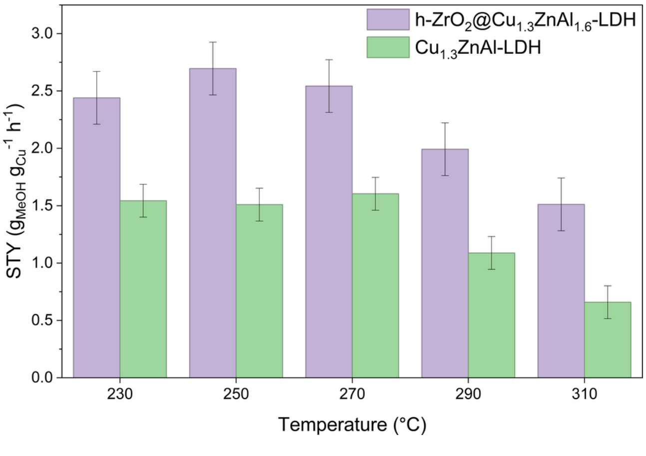

Figure 8. Catalytic data, reported per gram of copper, for $Cu_{1.3}$ZnAl-LDH and h-ZrO_2@$Cu_{1.3}ZnAl_{1.6}$-LDH (45 bar, 3:1 H_2:CO_2, WHSV = 18,000 mL g^{-1} h^{-1}).

The catalytic activity of the core@shell catalyst was compared to a physical mixture (PM) of the core and shell components. Since STEM-EDX and TGA data provide evidence of remaining AlOOH, h-ZrO_2@AlOOH was selected as the core component (rather than h-ZrO_2), with $Cu_{1.3}$ZnAl-LDH as the shell component. Surprisingly, similar catalytic performances were observed, despite the PM containing a greater amount of Al than the core@shell (Figure S21). This supports the claim that the precise quantity of Al present does not significantly influence the space-time yield, validating the earlier comparison of h-ZrO_2@$Cu_{1.3}ZnAl_{1.6}$-LDH to $Cu_{1.3}$ZnAl-LDH. The benefit of the core@shell structure, therefore, is that it is more uniform than a physical mixture, where insufficient mixing could lead to isolated regions of core or shell components. A greater sample uniformity is likely to minimize variations in catalytic performance, since synergistic benefits are likely to be enhanced by close proximity of components. Comparing the catalytic performance of the PM with $Cu_{1.3}$ZnAl-LDH alone provides evidence of synergy between the h-ZrO_2@AlOOH and LDH components: despite a lower proportion of the active LDH component, the PM still performs similarly to the LDH by itself.

The benefit of using a hollow core component is highlighted in Figure 9. Removing the inactive central SiO_2 sphere from the catalyst improves STY by a factor of approximately 1.3 at each temperature between 230 and 270 °C, when STY is considered on a per gram catalyst basis. This can be attributed to the higher CO_2 conversion (X_{CO2}) observed for the hollow core@shell structure than for the solid core@shell (Figure S22).

Direct comparison of catalytic performance to other studies is extremely challenging, owing to the extremely wide range of conditions employed in the literature (e.g., pressure, temperature, WHSV, reactor design). Nonetheless, the performance of activated h-ZrO_2@$Cu_{1.3}ZnAl_{1.6}$-LDH for CO_2 hydrogenation to methanol is highly competitive compared to other reported catalysts (Table S4).

Temperature programmed reduction using hydrogen (H_2-TPR) was used to probe for differences in Cu reducibility in the core@shell and LDH materials, providing insight into the superior activity observed for h-ZrO_2@$Cu_{1.3}ZnAl_{1.6}$-LDH. All samples were calcined in air at 330 °C prior to H_2-TPR experiments. No reduction events were observed in either h-ZrO_2 or h-ZrO_2@AlOOH (Figure S23).

The H_2-TPR profile of $Cu_{1.3}$ZnAl-LDH displays a single reduction event at 217 °C (Figure 10). In comparison, the profile of the PM (i.e., h-ZrO_2@AlOOH and $Cu_{1.3}$ZnAl-LDH) displays two reduction events, one at 234 °C and a lower temperature peak at 174 °C. The presence of this low temperature peak suggests that a hydrogen

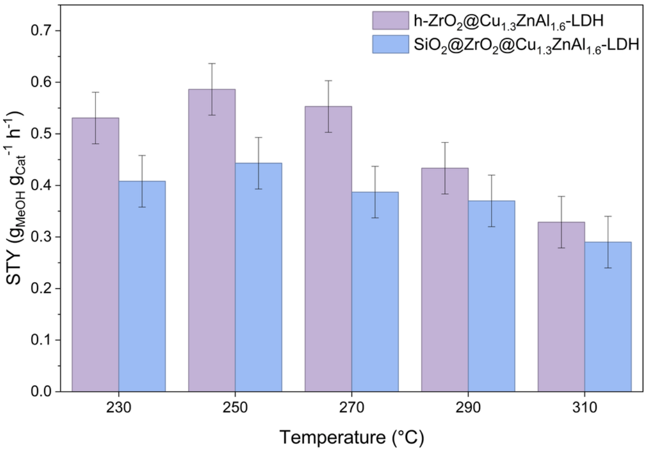

Figure 9. Catalytic testing data, reported per gram of the catalyst, for h-ZrO_2@$Cu_{1.3}ZnAl_{1.6}$-LDH compared to its solid-core counterpart, SiO_2@ZrO_2@$Cu_{1.3}ZnAl_{1.6}$-LDH (45 bar, 3:1 H_2:CO_2, WHSV = 18,000 mL g^{-1} h^{-1}).

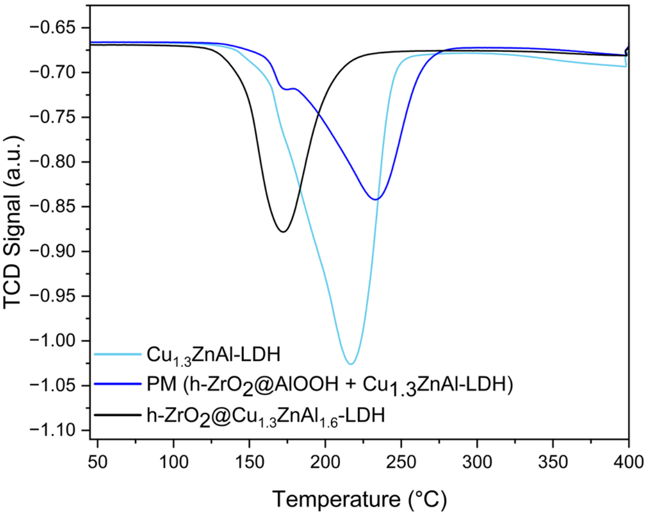

Figure 10. H_2-TPR profiles of h-ZrO_2@$Cu_{1.3}ZnAl_{1.6}$-LDH, $Cu_{1.3}$ZnAl-LDH, and the PM (h-ZrO_2@AlOOH + $Cu_{1.3}$ZnAl-LDH). The higher quantity of hydrogen consumed during the $Cu_{1.3}$ZnAl-LDH experiment (i.e., the larger area under the curve) compared to that in all other samples is attributed to its higher copper content: since equal sample masses were used in TPR experiments, the presence of h-ZrO_2@AlOOH (or h-ZrO_2) within a sample reduces the proportion of reducible copper.

spillover effect originating from h-ZrO_2@AlOOH aids Cu reduction in $Cu_{1.3}ZnAl_{1.6}$-LDH. Notably, this lower temperature peak is not observed for a mixture of h-ZrO_2 and $Cu_{1.3}$ZnAl-LDH (Figure S24), suggesting that the AlOOH layer is essential for enabling spillover, and does not negatively impact catalytic performance.

The H_2-TPR profile of h-ZrO_2@$Cu_{1.3}ZnAl_{1.6}$-LDH, on the other hand, displays a single broad peak at 170 °C, indicating that all of the Cu present is in the more reducible environment. The existence of this more reducible Cu environment in both the PM and core@shell samples is consistent with easier activation of Cu species and helps rationalize their improved performance relative to the LDH alone. In the case of the core@shell sample, h-ZrO_2@$Cu_{1.3}ZnAl_{1.6}$-LDH, the lower-temperature Cu reduction behavior combined with greater accessible Cu surface area (Table S2) are consistent with improved methanol synthesis performance arising from a more readily reducible, better-dispersed Cu environment. Direct identification of the active interfacial species in h-ZrO_2@$Cu_{1.3}ZnAl_{1.6}$-LDH, however, is challenging, as catalytically relevant Cu-ZnO-ZrO_2 interfacial species are expected to constitute only a fraction of the total Cu content. The similarity in activity between h-ZrO_2@$Cu_{1.3}ZnAl_{1.6}$-LDH and the PM, despite the much greater proportion of Cu in these more active sites, suggests that it is not these sites alone that are responsible for CO_2 hydrogenation, and another step in the CO_2 hydrogenation pathway, which is not dependent on Cu reducibility, has become limiting in the case of the core@shell.

Interestingly, the H_2-TPR profile of cp-h-ZrO_2+$Cu_{1.3}$ZnAl-LDH is almost identical to that of the PM, with only very small discrepancies in the temperatures of reduction events (Figure S25). This implies that: (i) only electrostatic interactions between the core and shell components exist within cp-h-ZrO_2+$Cu_{1.3}$ZnAl-LDH; (ii) the AlOOH coating enhances electrostatic interactions between the core and shell components (since a simple mixture of the h-ZrO_2@AlOOH and LDH components exhibits a similar reduction profile to that of cp-h-ZrO_2+$Cu_{1.3}$ZnAl-LDH, which itself is distinct from a mixture of h-ZrO_2 and $Cu_{1.3}$ZnAl-LDH); (iii) AlOOH is crucial for making a core@shell structure, as only co-precipitation of the LDH onto h-ZrO_2@AlOOH results in a single, low-temperature H_2-TPR peak.

■ CONCLUSIONS

This work presents the design of a h-ZrO_2@$Cu_{1.3}ZnAl_{1.6}$-LDH core@shell system for direct CO_2 hydrogenation to methanol. Despite >50% reduction in copper loading, h-ZrO_2@$Cu_{1.3}ZnAl_{1.6}$-LDH exhibits a similar performance to a commercial catalyst when considered on a per gram catalyst basis (0.59 g_{MeOH} g_{cat}^{-1} h^{-1}). The enhanced catalytic efficiency of h-ZrO_2@$Cu_{1.3}ZnAl_{1.6}$-LDH is highlighted when activity is per unit mass of copper, outperforming the industrial catalyst by a factor of two across all temperatures studied. Through various characterization techniques, we have demonstrated that h-ZrO_2@$Cu_{1.3}ZnAl_{1.6}$-LDH displays a distinct structure from a physical mixture of the core and shell components, and coating h-ZrO_2 in AlOOH before performing the co-precipitation is important in facilitating the formation of a core@shell structure. Future *operando* spectroscopic studies targeted at interfacial Cu species will be required to identify the active sites more directly.

■ ASSOCIATED CONTENT

Supporting Information

The Supporting Information is available free of charge at https://pubs.acs.org/doi/10.1021/acscatal.6c01304.

> TEM images and EDX maps of h-ZrO_2, size distributions of SiO_2 and ZrO_2 layer thickness, SEM-EDX of an unsuccessful SiO_2@ZrO_2 synthesis, Rietveld refinement of calcined SiO_2@ZrO_2, STEM-EDX maps of h-ZrO_2@$Cu_{1.3}ZnAl_{1.6}$-LDH and cp-h-ZrO_2+$Cu_{1.3}$ZnAl-LDH, solid-state ^{29}Si NMR spectra of SiO_2@ZrO_2 and h-ZrO_2, zeta potential measurements of the LDH and h-ZrO_2, PXRD patterns of activated h-ZrO_2@$Cu_{1.3}ZnAl_{1.6}$-LDH, BJH pore sizes of h-ZrO_2 and h-ZrO_2@AlOOH, post-testing TEM image, additional catalytic testing and H_2-TPR data, comparative performance table of literature catalysts and tables of ICP-OES, S_{Cu}, D_{Cu}, and CO_2-TPD data (PDF)

AUTHOR INFORMATION

Corresponding Author

Dermot O'Hare – *Chemistry Research Laboratory, University of Oxford, Mansfield Road, Oxford OX1 3TA, United Kingdom;* orcid.org/0000-0001-8054-8751; Email: dermot.ohare@chem.ox.ac.uk

Authors

Emma L. Southall – *Chemistry Research Laboratory, University of Oxford, Mansfield Road, Oxford OX1 3TA, United Kingdom;* orcid.org/0000-0002-6087-6923

Gerardo T. Martinez – *Department of Materials, University of Oxford, Parks Road, Oxford OX1 3PH, United Kingdom;* orcid.org/0000-0001-5036-0491

Roland C. Turnell-Ritson – *Chemistry Research Laboratory, University of Oxford, Mansfield Road, Oxford OX1 3TA, United Kingdom;* orcid.org/0000-0003-3702-9467

Complete contact information is available at:
https://pubs.acs.org/doi/10.1021/acscatal.6c01304

Author Contributions

The manuscript was written through contributions of all authors. All authors have given approval to the final version of the manuscript. E.L.S. performed experimental work and characterization, G.T.M. performed high-resolution STEM-EDX, R.C.T.-R. supervised the research, D.O'H. conceptualized and supervised the research and acquired funding.

Funding

SCG Chemicals Public Co., Ltd (Thailand).

Notes

The authors declare no competing financial interest.

ACKNOWLEDGMENTS

E.L.S., R.C.T.-R., and D.O'H. would like to thank SCG Chemicals Public Co., Ltd. (Thailand) for funding. The authors acknowledge use of characterization facilities within the David Cockayne Centre for Electron Microscopy, Department of Materials, University of Oxford, alongside financial support provided by the Henry Royce Institute (Grant ref EP/R010145/1). Dr. Nicholas Rees is thanked for performing SS-NMR spectroscopy experiments. Synchrotron data were collected on the I11 beamline at Diamond Light Source, UK. Access was provided via the block allocation group (CY39378).

ABBREVIATIONS

LDH	layered double hydroxide
h-ZrO_2	hollow zirconia spheres
STY	space-time yield
WHSV	weight hourly space velocity
CCU	carbon capture and utilisation
CTM	carbon dioxide to methanol
IEA	International Energy Agency
AMOST	aqueous-miscible organic solvent treatment
TEM	transmission electron microscopy
EDX	energy dispersive X-ray
NMR	nuclear magnetic resonance
BJH	Barrett-Joyner-Halenda
CZA	copper-zinc-aluminum
STEM	scanning transmission electron microscopy
PM	physical mixture
ICP-OES	inductively coupled plasma optical emission spectroscopy
TGA	thermogravimetric analysis
dTGA	first derivative of the thermogravimetric data
X_{CO2}	CO_2 conversion
H_2-TPR	hydrogen temperature programmed reduction
PXRD	powder X-ray diffraction.

REFERENCES

(1) Kim, C.; Yoo, C.-J.; Oh, H.-S.; Min, B. K.; Lee, U. Review of carbon dioxide utilization technologies and their potential for industrial application. *J. CO2 Util.* **2022**, *65*, No. 102239 .

(2) *World's Largest CO_2-To-Methanol Plant Starts Production*; Carbon Recycling International, https://carbonrecycling.com/about/news/co2-to-methanol-reactor-installed-in-anyang (accessed 2026-04-16).

(3) *Pilot plant uses CO2 for synthesizing methanol*; Mitsubishi Power Europe, https://power.mhi.com/regions/emea/news/2019/20190528.html (accessed 2026-04-16).

(4) *Kassø e-methanol facility*; European Energy, https://europeanenergy.com/kasso/ (accessed 2026-04-16).

(5) *Completion of CCU Pilot Facility for Demonstration of the Technology as a Green Innovation Fund Project*; Sumitomo Chemical, https://www.sumitomo-chem.co.jp/english/news/detail/20231212e.html (accessed 2026-04-16).

(6) Tabibian, S. S.; Sharifzadeh, M. Statistical and analytical investigation of methanol applications, production technologies, value-chain and economy with a special focus on renewable methanol. *Renewable Sustainable Energy Rev.* **2023**, *179*, No. 113281.

(7) Fasihi, M.; Breyer, C. Global production potential of green methanol based on variable renewable electricity. *Energy Environ. Sci.* **2024**, *17* (10), 3503–3522.

(8) Beck, A.; Newton, M. A.; van de Water, L. G. A.; van Bokhoven, J. A. The Enigma of Methanol Synthesis by $Cu/ZnO/Al_2O_3$-Based Catalysts. *Chem. Rev.* **2024**, *124* (8), 4543–4678.

(9) Agyekum, E. B.; Okonkwo, P. C.; Rashid, F. L. Research on biomass energy and CO_2 conversion to methanol: a combination of conventional and bibliometric review analysis. *Carbon Res.* **2025**, *4* (1), 4.

(10) Li, Q.; Khosravi, A.; Farsaei, A.; Sun, L. Thermodynamics, economic and carbon emission analysis of power-to-methanol process through alkaline electrolysis and monoethanolamine (MEA) carbon capture. *Chem. Eng. Sci.* **2024**, *293*, No. 120029.

(11) Jiang, X.; Nie, X.; Guo, X.; Song, C.; Chen, J. G. Recent Advances in Carbon Dioxide Hydrogenation to Methanol via Heterogeneous Catalysis. *Chem. Rev.* **2020**, *120* (15), 7984–8034 .

(12) Zhao, J.; Qin, B.; Zhang, Z.; Zhu, S.; Wu, G.; Li, J.; Chai, Y.; Li, L. Zeolite-stabilized trinuclear Zn_1Cu_2 sites catalyze CO_2 hydrogenation to methanol. *Chem* **2026**, *12* (2), No. 102743.

(13) Tang, A.; Wu, G.; Chai, Y.; Li, L. CO_2 Selective Hydrogenation to Methanol Catalyzed by CuZn Active Sites Confined in Silicalite-1 Zeolite. *ACS Catal.* **2025**, *15* (23), 19984–19993.

(14) Fujitani, T.; Nakamura, J. The effect of ZnO in methanol synthesis catalysts on Cu dispersion and the specific activity. *Catal. Lett.* **1998**, *56* (2), 119–124.

(15) Liao, F.; Huang, Y.; Ge, J.; Zheng, W.; Tedsree, K.; Collier, P.; Hong, X.; Tsang, S. C. Morphology-Dependent Interactions of ZnO with Cu Nanoparticles at the Materials' Interface in Selective Hydrogenation of CO_2 to CH_3OH. *Angew. Chem., Int. Ed.* **2011**, *50* (9), 2162–2165.

(16) *Diversification is the cornerstone of energy security, yet critical minerals are moving in the opposite direction*; IEA, https://www.iea.org/news/diversification-is-the-cornerstone-of-energy-security-yet-critical-minerals-are-moving-in-the-opposite-direction (accessed 2026-04-16).

(17) Zhang, H.; Chen, J.; Han, X.; Pan, Y.; Hao, Z.; Tang, S.; Zi, X.; Zhang, Z.; Gao, P.; Li, M.; Lv, J.; Ma, X. High-Performance Cu/ZnO/Al_2O_3 Catalysts for CO_2 Hydrogenation to Methanol. *Ind. Eng. Chem. Res.* **2024**, *63* (14), 6210–6221.

(18) Cui, X.; Luo, M.; Yang, Z.; Rahman, R.; Li, Z.; Yang, W.; Xia, L. Efficient Cu−Zn−Al/LDH Catalysts for CO_2-to-Methanol Conversion. *Energy Fuels* **2025**, *39* (5), 2675–2687.

(19) Evans, D. G.; Slade, R. C. T.Structural Aspects of Layered Double Hydroxides. In *Layered Double Hydroxides*; Duan, X., Evans, D. G., Eds.; Springer Berlin Heidelberg: Berlin Heidelberg, **2006**; pp 1–87.

(20) Lyu, M.; Zheng, J.; Coulthard, C.; Ren, J.; Zhao, Y.; Tsang, S. C. E.; Chen, C.; O'Hare, D. Core−shell silica@Cu_xZnAl LDH catalysts for efficient CO_2 hydrogenation to methanol. *Chem. Sci.* **2023**, *14* (36), 9814–9819.

(21) Li, M. M. J.; Chen, C.; Ayvalı, T.; Suo, H.; Zheng, J.; Teixeira, I. F.; Ye, L.; Zou, H.; O'Hare, D.; Tsang, S. C. E. CO_2 Hydrogenation to Methanol over Catalysts Derived from Single Cationic Layer CuZnGa LDH Precursors. *ACS Catal.* **2018**, *8* (5), 4390–4401.

(22) Zhang, L. H.; Zheng, C.; Li, F.; Evans, D. G.; Duan, X. Copper-containing mixed metal oxides derived from layered precursors: control of their compositions and catalytic properties. *J. Mater. Sci.* **2008**, *43* (1), 237–243.

(23) Wang, Q.; O'Hare, D. Large-scale synthesis of highly dispersed layered double hydroxide powders containing delaminated single layer nanosheets. *Chem. Commun.* **2013**, *49* (56), 6301–6303.

(24) Chen, C.; Felton, R.; Buffet, J.-C.; O'Hare, D. Core−shell SiO_2@LDHs with tuneable size, composition and morphology. *Chem. Commun.* **2015**, *51* (16), 3462–3465.

(25) Kondratowicz, T.; Gajewska, M.; Li, J.; Li, M. M.-J.; Turner, Z. R.; Chen, C.; O'Hare, D. Hollow-SiO_2@$Cu_xZn_yMg_z$Al-LDHs as catalyst precursors for CO_2 hydrogenation to methanol. *Chem. Sci.* **2025**, *16* (3), 1327–1335.

(26) Ren, S.; Fan, X.; Shang, Z.; Shoemaker, W. R.; Ma, L.; Wu, T.; Li, S.; Klinghoffer, N. B.; Yu, M.; Liang, X. Enhanced catalytic performance of Zr modified CuO/ZnO/Al_2O_3 catalyst for methanol and DME synthesis via CO_2 hydrogenation. *J. CO2 Util.* **2020**, *36*, 82–95.

(27) Gao, P.; Li, F.; Zhan, H.; Zhao, N.; Xiao, F.; Wei, W.; Zhong, L.; Wang, H.; Sun, Y. Influence of Zr on the performance of Cu/Zn/Al/Zr catalysts via hydrotalcite-like precursors for CO_2 hydrogenation to methanol. *J. Catal.* **2013**, *298*, 51–60.

(28) Li, K.; Chen, J. G. CO_2 Hydrogenation to Methanol over ZrO_2-Containing Catalysts: Insights into ZrO_2 Induced Synergy. *ACS Catal.* **2019**, *9* (9), 7840–7861.

(29) Luo, P.; Shi, P.; Yan, Z.; Han, J.; Wang, J.; Li, Y.; Ban, H.; Cai, W.; Li, C. Ternary synergistic interaction of Cu-ZnO-ZrO_2 promoting CO_2 hydrogenation to methanol. *Appl. Catal. A* **2025**, *689*, No. 120006.

(30) Sato, S.; Takahashi, R.; Sodesawa, T.; Yuma, K.-i.; Obata, Y. Distinction between Surface and Bulk Oxidation of Cu through N_2O Decomposition. *J. Catal.* **2000**, *196* (1), 195–199.

(31) Kondratowicz, T.; Drozdek, M.; Rokicińska, A.; Natkański, P.; Michalik, M.; Kuśtrowski, P. Novel CuO-containing catalysts based on ZrO_2 hollow spheres for total oxidation of toluene. *Microporous Mesoporous Mater.* **2019**, *279*, 446–455.

(32) Arnal, P. M.; Weidenthaler, C.; Schüth, F. Highly Monodisperse Zirconia-Coated Silica Spheres and Zirconia/Silica Hollow Spheres with Remarkable Textural Properties. *Chem. Mater.* **2006**, *18* (11), 2733–2739.

(33) Samson, K.; Śliwa, M.; Socha, R. P.; Góra-Marek, K.; Mucha, D.; Rutkowska-Zbik, D.; Paul, J. F.; Ruggiero-Mikołajczyk, M.; Grabowski, R.; Słoczyński, J. Influence of ZrO_2 Structure and Copper Electronic State on Activity of Cu/ZrO_2 Catalysts in Methanol Synthesis from CO_2. *ACS Catal.* **2014**, *4* (10), 3730–3741.

(34) Ma, Z.-Y.; Yang, C.; Wei, W.; Li, W.-H.; Sun, Y.-H. Catalytic performance of copper supported on zirconia polymorphs for CO hydrogenation. *J. Mol. Catal. A:Chem.* **2005**, *231* (1), 75–81.

(35) Zhang, X.; Yu, X.; Mendes, R. G.; Matvija, P.; Melcherts, A. E. M.; Sun, C.; Ye, X.; Weckhuysen, B. M.; Monai, M. Highly Dispersed ZnO Sites in a ZnO/ZrO_2 Catalyst Promote Carbon Dioxide-to-Methanol Conversion. *Angew. Chem., Int. Ed. Engl.* **2025**, *64* (4), No. e202416899.

(36) Luhmer, M.; d'Espinose, J. B.; Hommel, H.; Legrand, A. P. High-resolution ^{29}Si solid-state NMR study of silicon functionality distribution on the surface of silicas. *J. Magn. Reson. Imaging* **1996**, *14* (7), 911–913.

(37) Jo, W.-K.; Moru, S.; Tonda, S. A green approach to the fabrication of a TiO_2/NiAl-LDH core−shell hybrid photocatalyst for efficient and selective solar-powered reduction of CO_2 into value-added fuels. *J. Mater. Chem. A* **2020**, *8* (16), 8020–8032.

(38) Shao, M.; Ning, F.; Zhao, Y.; Zhao, J.; Wei, M.; Evans, D. G.; Duan, X. Core−Shell Layered Double Hydroxide Microspheres with Tunable Interior Architecture for Supercapacitors. *Chem. Mater.* **2012**, *24* (6), 1192–1197.

(39) Lyu, M.; Chen, C.; Buffet, J.-C.; O'Hare, D. A facile synthesis of layered double hydroxide based core@shell hybrid materials. *New J. Chem.* **2020**, *44* (24), 10095–10101.

(40) Scarpellini, D.; Leonardi, C.; Mattoccia, A.; Di Giamberardino, L.; Medaglia, P. G.; Mantini, G.; Gatta, F.; Giovine, E.; Foglietti, V.; Falconi, C.; Orsini, A.; Pizzoferrato, R. Solution-Grown Zn/Al Layered Double Hydroxide Nanoplatelets onto Al Thin Films: Fine Control of Position and Lateral Thickness. *J. Nanomater.* **2015**, *2015* (1), No. 809486.

(41) Ortiz-Ortiz, A. M.; Delgado Cornejo, D. O.; Fuelling, K. M.; Bielinski, A. R.; Ma, T.; Dasgupta, N. P. Tunable Growth of Layered Double Hydroxide Nanosheets through Hydrothermal Conversion of Atomic Layer Deposition Seed Layers. *Chem. Mater.* **2024**, *36* (17), 8300–8310.

(42) Mehrabadi, B. A. T.; Eskandari, S.; Khan, U.; White, R. D.; Regalbuto, J. R. Chapter One - A Review of Preparation Methods for Supported Metal Catalysts. In *Advance in Catalysis*; Song, C. Ed.; Elsevier, **2017**; pp. 1−35.

(43) Coelho, A. TOPAS and TOPAS-Academic: an optimization program integrating computer algebra and crystallographic objects written in C++. *J. Appl. Crystallogr.* **2018**, *51* (1), 210–218.

(44) Ram, S.; Singh, T. B.; Pathak, L. C. Synthesis and Thermogravimetric Analysis of Amorphous Boehmite Fibres. *Phys. Status Solidi A* **1998**, *165* (1), 151–164.

(45) Thomas, D.; Ranjan, R.; George, B. K. Co-Al-CO_3 layered double hydroxide: an efficient and regenerable catalyst for glycolysis of polyethylene terephthalate. *RSC Sustainability* **2023**, *1* (9), 2277–2286.

(46) Stangeland, K.; Li, H.; Yu, Z. Thermodynamic Analysis of Chemical and Phase Equilibria in CO_2 Hydrogenation to Methanol, Dimethyl Ether, and Higher Alcohols. *Ind. Eng. Chem. Res.* **2018**, *57* (11), 4081–4094.